Available online at www.sciencedirect.com

SciVerse ScienceDirect

Ceramics International 39 (2013) 4009–4016

CERAMICS INTERNATIONAL

www.elsevier.com/locate/ceramint

Iron-doped TiO_2 nanotubes with high photocatalytic activity under visible light synthesized by an ultrasonic-assisted sol-hydrothermal method

Xiuzhen Wei[a], Huijuan Wang[a], Guangfeng Zhu[a], Jinyuan Chen[a,*], Liping Zhu[b]

[a]*College of Biological and Environmental Engineering, Zhejiang University of Technology, No. 18 ChaoWang Rd., Hangzhou, China*
[b]*State Key Lab of Silicon Materials, Zhejiang University, Hangzhou 310027, China*

Received 21 September 2012; received in revised form 24 October 2012; accepted 26 October 2012
Available online 3 November 2012

Abstract

A series of iron-doped anatase TiO_2 nanotubes (Fe/TiO_2 NTs) catalysts with iron concentrations ranging from 0.88 to 7.00 wt% were prepared by an ultrasonic-assisted sol-hydrothermal process. The structures and the properties of the fabricated Fe/TiO_2 NTs were characterized in detail and photocatalytic activity was examined using a reactive brilliant red X-3B aqueous solution as pollutant under visible light. The lengths of the NTs were determined to range from 20 nm to 100 nm. The incorporation of the iron ions (Fe^{3+}) into the TiO_2 nanotubes shifted the photon absorbing zone from the ultraviolet (UV) to the visible wavelengths, reducing the band gap energy from 3.2 to 2.75 eV. The photocatalytic activity of the Fe/TiO_2 NTs was 2–4 times higher than the values measured for the pure TiO_2 nanotubes.

Keywords: Iron-doped; Ultrasonic; Catalytic properties; Microstructure

1. Introduction

Recently, titanium dioxide (TiO_2) has attracted considerable attention as a viable inorganic photocatalyst due to its unique biological and chemical properties as well as its cost-effectiveness [1–3]. TiO_2 has recently played an increased role in environmental treatment areas, such as air purification and wastewater treatment [4,5]. Despite these advantages as a photocatalyst, the wide band gap of TiO_2 (3.2 eV for the anatase phase and 3.0 eV for the rutile phase) requires the use of an ultraviolet (UV) excitation source, limiting its broad use in technological applications. When using natural sunlight as the TiO_2 excitation source, only ~5% of the incident radiation is used in the photocatalytic process [6,7]. To expand the applications for TiO_2 and to efficiently use solar light, processes to prepare TiO_2 nanotubes doped with suitable transition metallic or nonmetallic elements have been developed. Both non-metal elements, such as nitrogen [8], carbon [9], sulfur [10,11], boron [12], fluorine [13], and iodine [14], as well as metal elements, such as iron [15], cobalt [16], silver [17], and manganese [18], have been used to dope TiO_2 powders or nanotubes. These modifications have increased the photocatalytic activity of TiO_2 in the visible light range, as the combination probability of the photoinduced electron–hole pairs is minimized by doping with these elements. Among the various dopants, considerable research has focused on preparing Fe-doped TiO_2, as the radius of Fe^{3+} (0.64 Å) is similar to that of Ti^{4+} (0.68 Å) [19–25]. Fe-doped TiO_2 nanotubes have been reported to exhibit effective photocatalytic activity for organic pollutants degradation under visible light irradiation, as the Fe^{3+} ions act as shallow charge traps in the TiO_2 lattice [24].

To prepare the Fe/TiO_2 NTs, various methods, such as a sol–gel method [26], a template-based method [27], an electrochemical anodic oxidation of a pure titanium sheet [28], and a hydrothermal method [29] have been used. Recently, a sonochemical processing method was proved to be useful in generating novel materials with unusual

*Corresponding author. Tel./fax: +86 571 88320054.
E-mail address: cjy1128@zjut.edu.cn (J. Chen).

0272-8842/$ - see front matter © 2012 Elsevier Ltd and Techna Group S.r.l. All rights reserved.
http://dx.doi.org/10.1016/j.ceramint.2012.10.251

properties [30]. The acoustic cavitation effect derived from ultrasonic waves can result in the formation, growth and implosive collapse of sonochemical bubbles in a liquid, generating a high-temperature and high-pressure environment. These conditions can affect the morphology, the crystallinity and the photocatalytic activity of the TiO_2 nanotubes.

In this work, Fe/TiO_2 NTs were synthesized by an ultrasonic-assisted sol-hydrothermal method using tetrabutyl titanate ($C_{16}H_{36}O_4Ti$) as the precursors with $FeCl_3 \cdot 6H_2O$ as the dopant. The photocatalytic activity of the NTs under visible light irradiation was evaluated by measuring the degradation of a reactive brilliant red X-3B aqueous solution. To determine the relationship between the Fe content and the photocatalytic activity under visible light, XRD, BET, TEM, XPS, and UV–vis diffuse reflectance spectrum analyses were performed. This study may provide both useful information and an effective process for the preparation of TiO_2 nanotubes modified with either metallic or nonmetallic elements.

2. Experimental

2.1. Chemicals

The chemicals included hydrochloric acid (Zhejiang Quzhou Giant Reagent Co., Ltd.), absolute ethanol (Anhui Ante Biochemistry Co., Ltd.), nitrate (Zhejiang Star Chemical Reagent Co., Ltd.), sodium hydroxide (Hangzhou Xiaoshan Chemical Reagent Factory), tetrabutyl titanate ($C_{16}H_{36}O_4Ti$, Shanghai Star Chemical Co., Ltd. U.S.) and ferric chloride (National Pharmaceutical Group Chemical Reagent Co., Ltd.). All reagents were AR grade. Deionized water was used for all experiments.

2.2. Preparation of Fe/TiO_2 NTs

Fe/TiO_2 NTs were prepared by an ultrasonic-assisted sol-hydrothermal method. $C_{16}H_{36}O_4Ti$ was used as the titanium source, and an aqueous solution of ferric chloride ($FeCl_3 \cdot 6H_2O$) was used as the Fe source. Under constant stirring, 20 mL of tetrabutyl titanate was added to 80 mL absolute ethanol. After 20 min, 30 mL of nitrate and a 0.04 mol/L ferric chloride solution was added dropwise into the solution. After hydrolyzing the mixture at room temperature for 2 h under vigorous stirring, a transparent sol was obtained. The sol was then mixed with a 10 M NaOH solution and subjected to an ultrasonic-hydrothermal treatment. The treated sol was dispersed for 20 min with ultrasonic waves in a sealed Teflon-lined autoclave, followed by a treatment in an oven to allow for the reaction at the high temperature of 150 °C for 24 h. After the hydrothermal reaction, the product was cooled to room temperature. The precipitate was separated and rinsed thoroughly with both 0.1 mol/L HCl and distilled water until the pH value of the solution reached 7. The resulting product was dried at 80 °C. Using a heating rate of 5 °C/min in a chamber furnace (CWF 1100, CARBOLITE), the crystalline powder was calcined at 400 °C for 2 h. The nominal atomic ratios of Fe to Ti (R_{Fe}) were 0, 0.88, 1.75, 3.25, and 7 atomic% (at%) for the samples labeled R_0, $R_{0.88}$, $R_{1.75}$, $R_{3.25}$, and R_7, respectively.

2.3. Characterizations of the samples

The X-ray power diffraction (XRD) patterns were recorded with a D/max 2550 Pc automatic polycrystalline diffractometer (Cu Kα radiation, Rigaku-D/MAX-2500/PC, Japan) operating at 40 keV and 100 mA over the range $20 < 2\theta < 90^\circ$ with a scanning rate of 0.02°/s. The surface areas (S_{BET}) of the samples were analyzed by a multi-point Brunauer–Emmett–Teller (BET) method using nitrogen adsorption/desorption isotherm measurements at −196 °C on an ASAP 2010 nitrogen adsorption apparatus (Micromeritics Instruments, USA). Desorption isotherms were used to determine the pore size distribution using the Barret–Joyner–Halender (BJH) method [31,32]. Transmission electron microscopy (TEM) measurements using energy-dispersive X-ray spectrometry (EDX) were conducted with a Tecnai G2 F30 S-Twin electron microscope (Tecnai G2 F30 S-Twin, Holland) using a 300 kV accelerating voltage with a 0.20 nm point resolution. The X-ray photoelectron spectroscopy (XPS) measurements were performed on a PHI 5000C ESCA system with a Mg Kα source operating at 14.0 kV and 25 mA. The binding energies were referenced to the C 1s peak at 284.4 eV of the surface adventitious carbon. In addition, UV–vis spectra were obtained at room temperature with a UV–vis spectrophotometer (UV-2550, Shimadzu, Japan) using $BaSO_4$ as the reflectance standard for wavelengths between 240 nm and 800 nm.

2.4. Measurement of photocatalytic activity

Using visible light, the photocatalytic degradation activity of Fe/TiO_2 NTs was investigated using a simulated wastewater with reactive brilliant red X-3B solutions (20 mg/L). A glass reactor equipped with a xenon light source, which has a spectrum very close to that of sunlight, was used in these experiments.

The catalyst (100 mg of the NTs) was added to the reactive red X-3B simulated wastewater in the reactor equipped with the xenon light (Beijing Perfect Light Corporation, Beijing, China). To produce an adsorption and desorption equilibrium, the mixture was first stirred for 20 min (without any light irradiation), followed by irradiation with visible light. A small amount of the mixture was removed every 20 min and centrifuged. The separated limpid solution was used for an absorbance determination with a UV–vis spectrophotometer (TU-1810, Beijing, China). The photocatalytic activity of the samples was determined by analyzing the decrease in the X-3B concentration during the 2 h process.

3. Results and discussion

3.1. Crystal structure

XRD was used to identify and determine the phase structure, the crystallite size and the relative crystallinity of the samples. Fig. 1 presents the XRD patterns of the R_0 and $R_{1.75}$ NTs samples calcined at 400 °C. Both samples show peaks at the 2θ values of 25.4°, 37.6°, 48.3°, 54.2° and 62.7°, corresponding to the anatase (101), (004), (200), (211) and (204) crystal planes, respectively. The diffraction peaks belonging to the anatase phase in the $R_{1.75}$ NTs were greater than the corresponding peaks in the R_0 NTs. These results suggest that the Fe^{3+} ions used as dopants can accelerate the crystallization of the anatase phase and the growth of the crystallites, as previously reported [33,34]. Fig. 2 shows the XRD patterns of the NTs with various concentrations of the dopant Fe. Within the detection limit of this technique, all samples exhibited only the characteristic peaks of an anatase phase, indicating that the Fe^{3+} ions had entered into the titanate nanotube crystalline lattices rather than presented on the surface of the titanate nanotubes. Further observations demonstrated that the XRD peak intensities associated with the anatase structure increased with increasing R_{Fe} for values below 3%. For values of Fe reaching 7%, the diffraction peaks of the anatase phase can become weaker and slightly wider, suggesting a decrease in the crystallinity with the formation of smaller TiO_2 crystallites [35]. Even at the highest Fe concentrations, no crystalline phases containing Fe could be observed, indicating that the iron ions may be highly dispersed into the TiO_2. The XRD method was not sensitive enough to detect minor changes in the TiO_2 structure. As both Fe^{3+} (0.64 Å) and Ti^{4+} (0.68 Å) have similar ionic radius values, a Fe–TiO_2 solid solution may be formed from the Fe^{3+} substitution for Ti^{4+} within the crystal or at the interstices [36,37]. The small differences between the atomic size of the Fe and Ti ions may induce a deformation into the crystal lattice of TiO_2. As observed with the XRD results, for values of R_{Fe} higher than 1.75%, the Fe substitution decreased the crystallization of TiO_2, as reflected by a weaker diffraction intensity of the XRD pattern, and slightly restrained the growth of the TiO_2 crystallite.

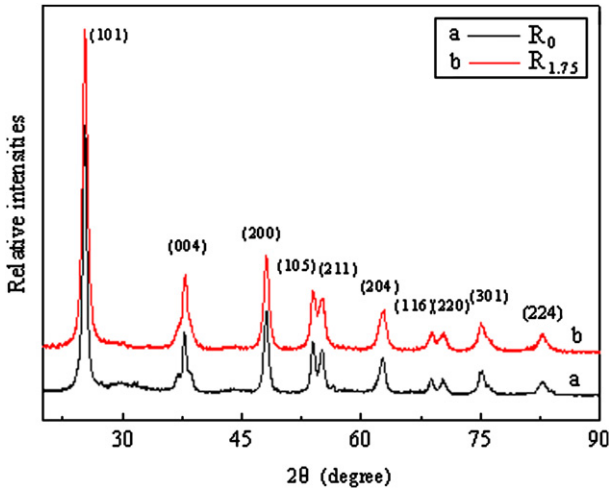

Fig. 1. XRD patterns of (a) R_0 NTs and (b) $R_{1.75}$ NTs.

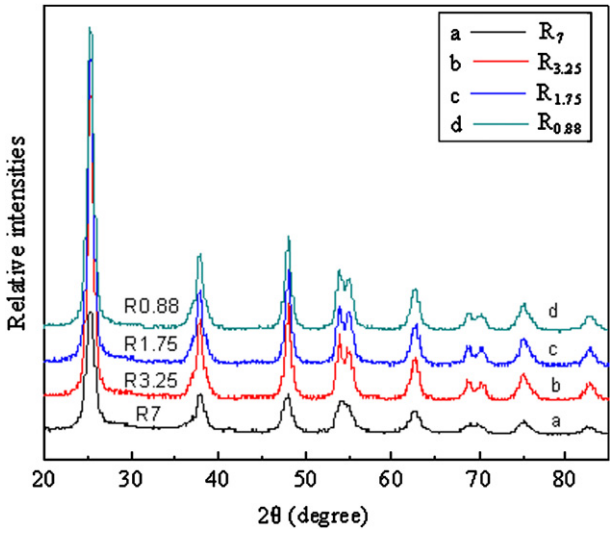

Fig. 2. XRD patterns of the Fe/TiO_2 NTs prepared at different R_{Fe} values.

3.2. BET surface area and pore distribution determination

Fig. 3 shows a representative plot of a nitrogen adsorption–desorption isotherm with pore size distribution curves (inset) for the $R_{1.75}$ NTs. The other NTs, which are not shown here, have similar isotherms and pore size distribution. The samples exhibited type IV isotherms with a type H3 hysteresis loop at relative pressures ranging from 0.6 to 1.0, indicating the presence of mesoporous structures [38]. The figure inset contains the pore size distribution of the $R_{1.75}$ NTs. The pore size distribution (inset) indicated a wide distribution range from 5 nm to over 50 nm. The pore volume of the pure and Fe/TiO_2 NTs prepared at R_{Fe}=0.88, 1.75, 3.25 and 7 were determined to be 1.11, 0.8, 0.95, 0.63 and 0.40 cm^3/g, respectively (see Table 1). As also shown in Table 1, the

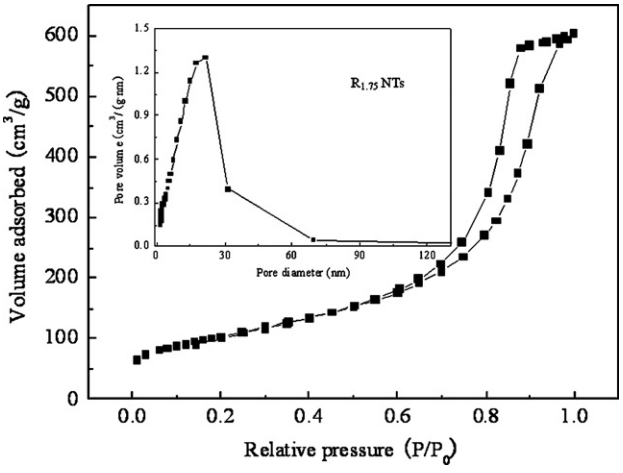

Fig. 3. Nitrogen adsorption–desorption isotherms and the corresponding pore size distribution curves (inset) of the $R_{1.75}$ NTs.

samples had relatively large surface areas. For R_{Fe} values greater than 1.75, the surface area, the pore volume and the average pore size decreased with increasing R_{Fe}, with the suppression of the crystallite growth. Nevertheless, decreased mesopore volumes were observed upon iron doping. High specific surface areas and pore volumes were obtained for iron content values of approximately 1.75, consistent with the results from the XRD measurements.

3.3. Morphology of the Fe/TiO_2 NTs

Fig. 4 shows the TEM images and the EDX of $R_{1.75}$ NTs prepared by an ultrasonic-assisted sol-hydrothermal method and calcined at 400 °C (see Section 2). As observed in the low-resolution TEM image in Fig. 4a, significant quantities of short nanotubes with lengths of several tens of nanometers were present. These nanotubes were created from the cavitations during the ultrasonic process that accelerate the sol particles to high velocities, leading to inter-particle collisions. Ultrasonic processes can generate high energy collisions, inducing the effective fusion and crystallization of the amorphous particles. As shown in Fig. 4b, the nanotube structure can be observed in the high-resolution images of the Fe/TiO_2 NTs, indicating that the prepared nanotubes are hollow and open-ended, and both of these features are beneficial in photocatalysis. The diameters of the nanotubes were nearly uniform with

Table 1
Summary of the physicochemical properties of the NTs.

Samples	Phase[a]	Band gap (eV)	Surface area (m^2/g)	Pore volume (cm^3/g nm)	Average pore size (nm)
Pure-NTs	A	3.19	484.4	1.11	9.24
R0.88	A	3.02	325	0.80	9.69
R1.75	A	2.95	370	0.95	10.1
R3.25	A	2.93	314	0.63	8.3
R7	A	2.75	263	0.40	5.9

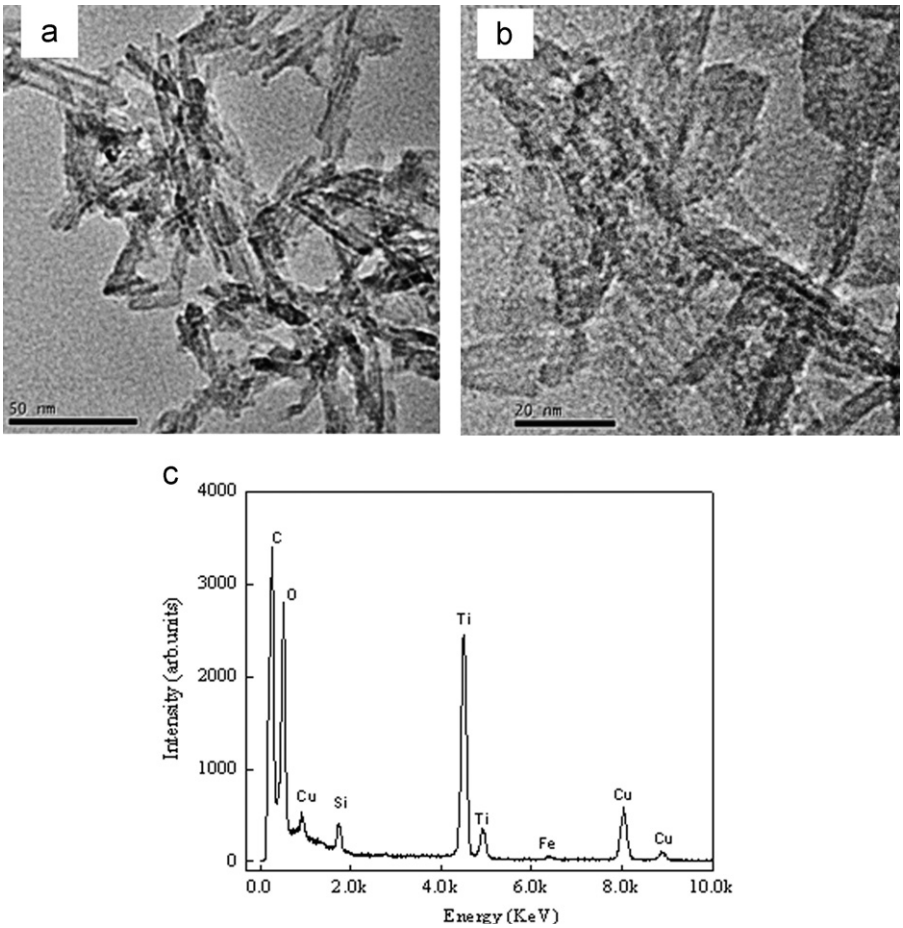

Fig. 4. TEM images of the Fe/TiO_2 NTs. (a) Low-magnification TEM images, (b) high-magnification TEM images, and (c) an EDX spectrum taken from the nanotubes shown in part b.

lengths of approximately 60 nm. The nanotube structures had outer diameters of approximately 8 nm.

Fig. 4c reveals the EDX spectrum obtained for the $R_{1.75}$ NTs that are shown in Fig. 4b. These spectra indicated that some doped Fe^{3+} ions were substituted into the octahedrally coordinated Ti^{4+} sites. Both Si and Cu were found in the EDX pattern, originating from the probe and the thin copper layer evaporated on the sample for the TEM characterization, respectively. Although sodium can be difficult to remove completely [39,40], no obvious sodium was detected in the samples.

3.4. XPS analysis

To analyze the chemical compositions of the prepared Fe–TiO_2 nanotubes and to identify the chemical status of the Fe element in the samples, the Fe/TiO_2 NTs were analyzed by XPS. Fig. 5a shows the XPS survey spectra of the Fe/TiO_2 NTs. The sharp peaks for Ti 2p, O 1s, Fe 2p, and C 1s are easily observed. The C 1s peak is at 282 eV. The residual carbon may be from the organic precursors and the adventitious hydrocarbon from the XPS instrument. To investigate the chemical states of both titanium and ferrum, high-resolution XPS spectra of both Ti 2p and Fe 2p were analyzed. As shown in Fig. 5b, both Ti $2p_{1/2}$ and Ti $2p_{3/2}$ spin-orbital splitting photoelectrons were located at 456.0 and 463.8 eV, indicating the presence of Ti^{4+}. An XPS scan of the Fe 2p core level is shown in Fig. 5c. Even with the low levels of doping, the Fe signal was observed. The binding energies located at approximately 708.6 ev and 721.5 ev were assigned to Fe^{3+} $2p_{3/2}$ and Fe^{3+} $2p_{1/2}$, respectively. The Fe elements in the samples existed mainly in the +3 oxidation state (Fe^{3+}). As the radii of Fe^{3+} (0.64 Å) and Ti^{4+} (0.68 Å) are similar, Fe^{3+} could be incorporated into the TiO_2 lattice to form the Ti–O–Fe bonds present in the Fe–TiO_2 nanotubes treated by calcination at 400 °C [41,42]. The concentration of the Fe dopant in the $R_{1.75}$ NTs analyzed by XPS was 2.6%. The initial nominal atomic ratio of $R_{1.75}$ was 1.75%, suggesting that the Fe dopant had a much higher concentration at the exterior than in the interior of the TiO_2. This phenomenon may have resulted from the hydrothermal doping treatment process. In the hydrothermal process, most Fe^{3+} ions can strongly absorb onto the surface of the TiO_2 gel due to the high surface area of the gel. The Fe^{3+} ions can diffuse gradually into the bulk of the TiO_2 grains by a substitution of the Ti^{4+} ions in the crystallization of the TiO_2 during the hydrothermal treatment process. As a result, the Fe^{3+} content decreases in the direction of the diffusion, that is, from the exterior to the interior [43].

3.5. UV–vis absorption spectra

The UV–vis diffuse reflectance spectra of the NTs with different Fe contents are shown in Fig. 6. The Fe/TiO_2 NTs demonstrated an appreciable shift with a strong absorption in the visible light region. The intensity of the visible absorbance of the NTs increased with increasing Fe content. Two components contributed to the enhanced absorptions in the visible region. The first component was from the excitation of the 3d electrons of Fe^{3+} to the TiO_2 conduction band (charge transfer transition) giving rise to a band centered at

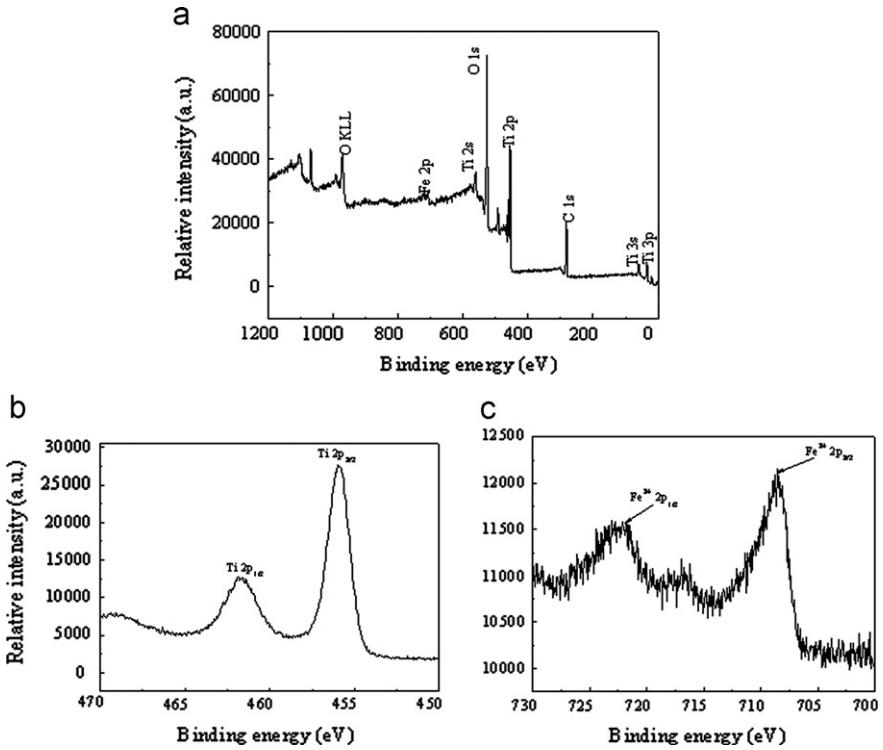

Fig. 5. XPS spectra of $1R_{1.75}$ NTs: (a) survey, (b) Ti 2p peaks, and (c) Fe 2p peaks.

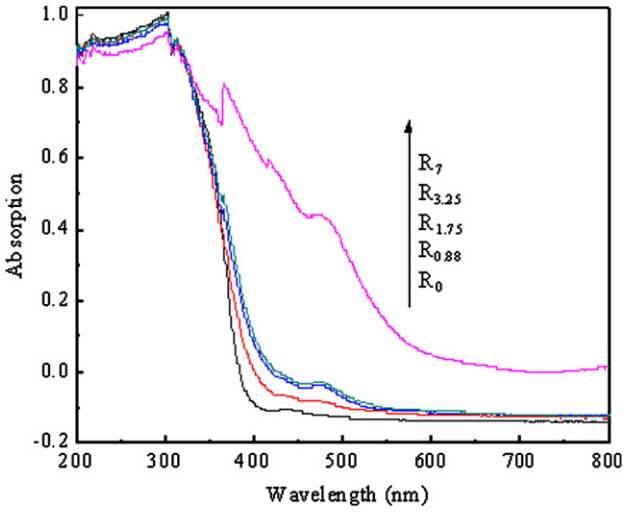

Fig. 6. UV–vis diffuse reflectance spectra of NTs prepared at the different values of R_{Fe}.

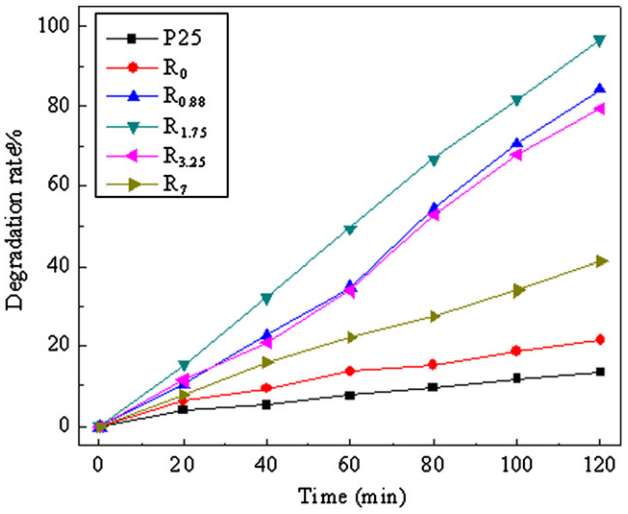

Fig. 7. Effect of the X-3B photodegradation using the NTs with various Fe doping concentrations.

approximately 400 nm. A band centered at approximately 500 nm was particularly apparent for the samples with the highest iron contents. This band may be attributed to the d–d transition of Fe^{3+} ($^2T_{2g} \rightarrow {}^2A_{2g}$, $^2T_{1g}$) or the charge transfer transition between the interacting iron ions ($Fe^{3+} + Fe^{3+} \rightarrow Fe^{4+} + Fe^{2+}$) [44]. These results suggest that the iron ions are indeed incorporated into the lattice of the TiO_2, altering both crystal and electronic structures. The band gaps of the samples can be calculated from the intercept of the UV–vis spectra using the equation, $E_g = 1240/\lambda$. The results are shown in Table 1. The band gap energies decreased with increasing Fe dopant concentrations, suggesting that the doped iron ions can be incorporated at a level near the valence band of the TiO_2, thus reducing the band gap [35].

3.6. Photocatalytic activities

Reactive brilliant X-3B was used as a model target pollutant to investigate the photocatalytic activity of the Fe-NTs upon visible light irradiation. Fig. 7 shows the degradation rate of X-3B in the presence of the Fe/TiO_2 NTs, pure NTs (undoped nanotubes) and P25 under visible light irradiation. The degradation rate of X-3B for P25 at 120 min was only 10%. The Fe/TiO_2 NTs had higher photocatalytic activities than did the pure NTs and P25. Three of the Fe/TiO_2 NTs $R_{1.75}$, $R_{0.88}$ and $R_{3.5}$, had higher photocatalytic activities than did R_7. The highest degradation rate for the Fe/TiO_2 NTs reached 96.5% within 120 min for the sample with the Fe dopant at 1.75%. The Fe^{3+} ions may have acted as traps to capture the photoinduced electrons and holes, thus inhibiting the recombination of the photoinduced electrons and holes and leading to an increase in the concentration of the photogenerated charge carrier. The photocatalytic activity of the Fe/TiO_2 NTs decreased for Fe dopant values at either high (7%) or low (0.88%) levels. The small amount of Fe^{3+} ions may have been insufficient to form the electronic accumulation center required for photocatalysis. For high concentrations of the iron dopant, a portion of the transition metal ions will become the combination center for the electrons and the holes. Of course, the crystallinity, the surface area, and the morphology can greatly influence the photocatalytic activity of the titania, which is widely believed to be phase-dependent. However, the influence of the phases was neglected in our experiments, as both the pure NTs and the Fe/TiO_2 NTs were in the anatase phase, which eliminates the variance in the photocatalytic activity that originate from the differences in the crystal phases.

For the Fe/TiO_2 NTs, the photocatalytic process generated using visible light may proceed using the following multi-step process. For the TiO_2 solutions irradiated with light, the conduction band electrons ($e-$) and the valence band holes ($h+$) are generated at the surface for the light energy values equaling or exceeding the band gap energy [45]. The holes can react with either the surface hydroxyl ions or water to produce hydroxyl radicals ($\cdot OH$). The electrons react with the adsorbed molecular oxygen to yield superoxide anion radicals ($\cdot O_2^-$) [46] that act as oxidizing agents, thus providing an additional source of the hydroxyl radicals. The hydroxyl radicals are strong oxidants that can react with the X-3B molecules, leading to the destruction of the X-3B. The detailed reaction steps of this degradation process are shown as follows: [47]

$$TiO_2 + h\nu(\text{visiblelight}) \rightarrow h^+(VB) + e^-(CB)$$

$$H_2O(\text{adsorbed}) + h^+(VB) \rightarrow \cdot OH(\text{adsorbed}) + H^+$$

$$X-3B(\text{adsorbed}) + (\cdot OH, \cdot O_2^-) \rightarrow \text{Mineralizedproducts}$$

4. Conclusions

TiO_2 nanotubes doped with upto 7 wt% Fe were prepared by an ultrasonic-assisted sol-hydrothermal method

using tetrabutyl titanate as the precursor and $FeCl_3 \cdot 6H_2O$ as the dopant. The results demonstrate that the Fe^{3+} ions caused changes in the phase composition, altering several properties of the catalyst, including the particle size and surface area as well as the photocatalytic activity. All of the Fe/TiO_2 NTs had higher photocatalytic activity than did the Degussa P25 and pure NTs, and the optimal doping concentration was determined to be $R_{Fe}=1.75$. Using visible light, the degradation rate of the X-3B for $R_{1.75}$ reached 96.5% within 120 min. Doping with Fe shifted the absorption edge of the NTs into the visible light range, thus reducing the band gap. The degradation rate of the reactive brilliant red X-3B using the Fe/TiO_2 NTs under visible light irradiation had a 2- to 4-fold increase over the pure NTs.

Acknowledgments

This work was supported by the Key Laboratory of Silicon Materials Program of China (SKL2010-18), the National Natural Science Foundation of China (No. 20877070 and 21177114) and the Zhejiang Provincial Natural Science Foundation of China (Y5080223).

References

[1] M.R. Hoffmann, S.T. Martin, W. Choi, D.W. Bahnemann, Environmental applications of semiconductor photocatalysis, Chemical Reviews 95 (1995) 69–96.
[2] Y. Yang, H. Wang, J.X. Li, B.Q. He, T.H. Wang, S.J. Liao, Novel functionalized nano-TiO_2 loading electrocatalytic membrane for oily wastewater treatment, Environmental Science and Technology 46 (2012) 6815–6821.
[3] U.I. Gaya, A.H. Abdullah, Most cited journal of photochemistry and photobiology C: photochemistry reviews articles, Journal of Photochemistry and Photobiology C: Photochemistry Reviews 9 (2008) 1–12.
[4] A.L. Linsebigler, G.Q. Lu, J.T. Yates, Photocatalysis on TiO_2 surfaces: principles, mechanisms and selected results, Chemical Reviews 95 (1995) 735–758.
[5] A. Fujishima, T.N. Rao, D.A. Tryk, Titanium dioxide photocatalysis, Journal of Photochemistry and Photobiology C: Photochemistry Reviews 1 (2000) 1–21.
[6] X.B. Chen, S.S. Mao, Titanium dioxide nanomaterials: synthesis, properties, modifications, and applications, Chemical Reviews 107 (2007) 2891–2959.
[7] M. Anpo, Preparation characterization and reactivates of highly functional titanium oxide-based photocatalysts able to operate under UV–visible light irradiation: approaches in realizing high efficiency in the use of visible light, Bulletin of the Chemical Society of Japan 77 (2004) 1427–1442.
[8] M.C. Wang, H.J. Lin, C.H. Wang, H.C. Wu, Effects of annealing temperature on the photocatalytic of N-doped TiO_2 thin films, Ceramics International 38 (2012) 195–200.
[9] T.H.T. Vu, T.T.T. Nguyen, P.H.T. Nguyen, M.H. Do, H.T. Au, T.B. Nguyen, D.L. Nguyen, J.S. Park, Fabrication of photocatalytic composite of multi-walled carbon nanotubes/TiO_2 and its application for desulfurization of diesel, Materials Research Bulletin 47 (2012) 308–314.
[10] Y.M. Liu, J.Z. Liu, Y.L. Lin, Y.F. Zhang, Y. Wei, Simple fabrication and photocatalytic activity of S-doped TiO_2 under low power LED visible light irradiation, Ceramics International 35 (2009) 3061–3065.
[11] H. Tian, J.F. Ma, K. Li, J.J. Li, Hydrothermal synthesis of S-doped TiO_2 nanoparticles and their photocatalytic ability for degradation of methyl orange, Ceramics International 35 (2009) 1289–1292.
[12] J.Y. Li, N. Lu, X. Quan, S. Chen, H.M. Zhao, Facile method for fabricating boron-doped TiO_2 nanotube array with enhanced photoelectrocatalytic properties, Industrial and Engineering Chemistry Research 47 (2008) 3804–3808.
[13] H. Jiang, H. Song, Z. Zhou, X. Liu, G. Meng, Characterization of LiF-doped TiO_2 and its photocatalytic activity for decomposition of trichloromethane, Materials Research Bulletin 43 (2008) 3037–3046.
[14] Y. Su, Y. Xiao, X. Fu, Y. Deng, F. Zhang, Photocatalytic properties and electronic structures of iodine-doped TiO_2 nanotubes, Materials Research Bulletin 44 (2009) 2169–2173.
[15] H. Yu, H. Irie, Y. Shimodaira, Y. Hosogi, Y. Kuroda, M. Miyauchi, K. Hashimoto, An efficient visible-light-sensitive Fe (III) grafted TiO_2 photocatalyst, Journal of Physical Chemistry C 114 (2010) 16481–16487.
[16] J. Kuljanin-Jakovljevic, M. Radoicic, T. Radetic, Z. Konstantinovic, Z.V. Saponjic, J. Nedeljkovic, Presence of room temperature ferromagnetism in Co^{2+} doped TiO_2 nanoparticles synthesized through shape transformation, Journal of Physical Chemistry C 113 (2009) 21029–21033.
[17] C. Suwanchawalit, S. Wongnawa, P. Sriprang, P. Meanha, Enhancement of the photocatalytic performance of Ag-modified TiO_2 photocatalyst under visible light, Ceramics International 38 (2012) 5201–5207.
[18] G. Shao, Electronic structures of manganese-doped rutile TiO_2 from first principles, Journal of Physical Chemistry C 112 (2008) 18677–18685.
[19] M.P. Seabra, I.M.M. Salvado, J.A. Labrincha, Pure and (zinc or rion) doped titania powders prepared by sol–gel and used as photocatalyst, Ceramics International 37 (2001) 3317–3322.
[20] K. Melghit, O.S. Al-Shukeili, I. Ai-Amri, Effect of M-deping (M=Fe, V) on the photocatalytic activity of nanorod rutile TiO_2 for congo red degradation under the sunlight, Ceramics International 35 (2009) 433–439.
[21] A. Kumbhar, G. Chumanov, Synthesis of iron (III)-doped titania nanoparticles and its application for photodegradation of sulforhodamine-B pollutant, Journal of Nanoparticle Research 7 (2005) 489–498.
[22] M.H. Zhou, J.G. Yu, B. Cheng, H.G. Yu, Preparation and photocatalytic activity of Fe-doped mesoporous titanium dioxide nanocrystalline photocatalysts, Materials Chemistry and Physics 93 (2005) 159–163.
[23] X.H. Wang, J.G. Li, H. Kamiyama, Y. Moriyoshi, T. Ishigaki, Wavelength-sensitive photocatalytic degradation of methyl orange in aqueous suspension over iron (III)-doped TiO_2 nanopowders under UV and visible light irradiation, Journal of Physical Chemistry B 110 (2006) 6804–6809.
[24] J.F. Zhu, F. Chen, J.L. Zhang, H.J. Chen, M. Anpo, Fe^{3+}–TiO_2 photocatalysts prepared by combining sol–gel method with hydrothermal treatment and their characterization, Journal of Photochemistry and Photobiology A 180 (2006) 196–204.
[25] E. Piera, M.I. Tejedor-Tejedor, M.E. Zorn, M.A. Anderson, Relationship concerning the nature and concentration of Fe (III) species on the surface of TiO_2 particles and photocatalytic activity of the catalyst, Applied Catalysis B 46 (2003) 671–685.
[26] T. Maiyalagan, B. Viswanathan, U.V. Varadaraju, Fabrication and characterization of uniform TiO_2 nanotube arrays by sol–gel template method, Bulletin of Material Science 29 (2006) 705–708.
[27] I. Tacchini, E. Terrado, A. Anson, M.T. Martinez, Anatase nanotubes synthesized by a template method and their application as a green photocatalyst, Journal of Materials Science 46 (2011) 2097–2104.
[28] D.V. Portan, K. Papaefthymiou, E. Arvanita, G. Jiga, G.C. Papanicolaou, A combined statistical and microscopic analysis of TiO_2 nanotubes synthesized under different electrochemical anodizing conditions, Journal of Materials Science 47 (2012) 4696–4705.

[29] A. Nakahira, T. Kubo, C. Numako, Formation mechanism of TiO_2-derived titanate nanotubes prepared by the hydrothermal process, Inorganic Chemistry 49 (2010) 5845–5852.
[30] P. Jeevanandam, Y. Koltypin, Y. Mastai, A. Gedanken, Sonochemical synthesis of lead hydroxy bromide needles, Journal of Materials Chemistry 10 (2000) 2143–2146.
[31] K.S.W. Sing, D.H. Everett, R. Haul, L. Moscou, R.A. Pierotti, J. Rouquérol, T. Siemieniewska, Reporting physisorption data for gas/solid interface with special reference to the determination of surface area and porosity, Pure and Applied Chemistry 54 (1982) 2201–2218.
[32] J.G. Yu, J.C. Yu, M.K.P. Leung, W.K. Ho, B. Cheng, X.J. Zhao, J.C. Zhao, Effects of acidic and basic hydrolysis catalysts on the photocatalytic activity and microstructures of bimodal mesoporous titania, Journal of Catalysis 217 (2003) 69–78.
[33] Z.B. Zhang, C.C. Wang, R. Zakaria, J.K. Ying, Role of particle size in nanocrystalline TiO_2-based photocatalysts, Journal of Physical Chemistry B 102 (1998) 10871–10878.
[34] Y. Cong, J.L. Zhang, F. Chen, M. Anpo, D.N. He, Preparation, photocatalytic activity and mechanism of nano-TiO_2 co-doped with nitrogen and iron (III), Journal of Physical Chemistry C 111 (2007) 10618–10623.
[35] J.G. Yu, Q.J. Xiang, M.H. Zhou, Preparation, characterization and visible-light-driven photocatalytic activity of Fe-doped titania nanorods and first-principles study for electronic structures, Applied Catalysis B 90 (2009) 595–602.
[36] C.A. Castro-López, A. Centeno, S.A. Giraldo, Fe-modified TiO_2 photocatalysts for the oxidative degradation of recalcitrant water contaminants, Catalysis Today 157 (2010) 119–124.
[37] C.Y. Wang, C. Bottcher, D.W. Bahneman, J.K. Dohrman, A comparative study of nanometer sized Fe (III)-doped TiO_2 photocatalysts: synthesis, characterization and activity, Journal of Materials Chemistry 13 (2003) 2322–2329.
[38] J.G. Yu, H.G. Yu, B. Cheng, C. Trapalis, Effects of calcination temperature on the microstructures and photocatalytic activity of titanate nanotubes, Journal of Molecular Catalysis A: Chemical 249 (2006) 135–142.
[39] R. Ma, Y. Bando, T. Sasaki, Nanotubes of lepidocrocite titanates, Chemical Physics Letters 380 (2003) 577–582.
[40] X. Sun, Y. Li, Synthesis and characterization of ion-exchangeable titanate nanotubes, Chemistry European Journal 9 (2003) 2229–2238.
[41] P. Zhang, S. Yin, T. Sato, Synthesis of iron-containing nitrogen-doped titania by hydrothermal method and its photocatalytic activity, Research on Chemical Intermediates 37 (2011) 479–485.
[42] J.G. Yu, H.G. Yu, C.H. Ao, S.C. Lee, J.C. Yu, W.K. Ho, Preparation, characterization and photocatalytic activity of in situ Fe-doped TiO_2 thin films, Thin Solid Films 496 (2006) 273–280.
[43] L. Deng, S. Wang, D. Liu, B. Zhu, W. Huang, S. Wu, S. Zhang, Synthesis, characterization of Fe-doped TiO_2 nanotubes with high photocatalytic activity, Catalysis Letters 129 (2009) 513–518.
[44] C. Adán, A. Bahamonde, M. Fernández-García, A. Martínez-Arias, Structure and activity of nanosized iron-doped anatase TiO_2 catalysts for phenol photocatalytic degradation, Applied Catalysis B 72 (2007) 11–17.
[45] T.Y. Han, C.F. Wu, C.T. Hsieh, Hydrothermal synthesis and visible light photocatalysis of metal-doped titania nanoparticles, Journal of Vacuum Science and Technology B 25 (2007) 430–435.
[46] Y.F. Tu, S.Y. Huang, J.P. Sang, X.W. Zou, Preparation of Fe-doped TiO_2 nanotube arrays and their photocatalytic activities under visible light, Materials Research Bulletin 45 (2010) 224–229.
[47] N. Bao, Y. Li, Z.T. Wei, G.B. Yin, J.J. Niu, Adsorption of dyes on hierarchical mesoporous TiO_2 fibers and its enhanced photocatalytic properties, Journal of Physical Chemistry C 115 (2011) 5708–5719.